

RadioAstron Science Program Five Years after Launch: Main Science Results

N. S. Kardashev^{a,*}, A. V. Alakoz^a, A. S. Andrianov^a, M. I. Artyukhov^b, W. Baan^c, V. E. Babyshkin^b, N. Bartel^d, O. S. Bayandina^a, I. E. Val'tts^a, P. A. Voitsik^a, A. Z. Vorobyov^b, C. Gwinn^e, J. L. Gomez^f, G. Giovannini^g, D. Jauncey^h, M. Johnsonⁱ, H. Imai^j, Y. Y. Kovalev^a, S. E. Kurtz^k, M. M. Lisakov^a, A. P. Lobanov^l, V. A. Molodtsov^b, B. S. Novikov^a, A. V. Pogodin^b, M. V. Popov^a, A. S. Privesenzev^b, A. G. Rudnitski^a, G. M. Rudnitski^m, T. Savolainenⁿ, T. V. Smirnova^o, A. M. Sobolev^p, V. A. Soglasnov^a, K. V. Sokolovsky^a, E. N. Filippova^b, V. V. Khartov^b, M. E. Churikova^b, A. E. Shirshakov^b, V. I. Shishov^o, and P. Edwards^q

^a*Astro Space Center, Lebedev Physical Institute, Russian Academy of Sciences, Moscow, Russia*

^b*Lavochkin Scientific and Production Association, Khimki, Moscow oblast, Russia*

^c*ASTRON Netherlands Institute for Radio Astronomy, Dwingeloo, the Netherlands*

^d*Department of Physics and Astronomy, York University, Toronto, Canada*

^e*University of California at Santa Barbara, Santa Barbara, California, United States*

^f*Institute of Astrophysics of Andalusia, Granada, Andalusia, Spain*

^g*Department of Physics and Astronomy, University of Bologna, Bologna, Italy*

^h*Research School of Astronomy and Astrophysics, Australian National University, Canberra, Australia*

ⁱ*Harvard–Smithsonian Center for Astrophysics, Cambridge, Massachusetts, United States*

^j*Graduate School of Science and Engineering, Kagoshima University, Kagoshima, Japan*

^k*Center for Radio Astronomy and Astrophysics, Nacional Autonomous University of Mexico, Morelia, Mexico*

^l*Max-Planck-Institute for Radio Astronomy, Bonn, Germany*

^m*Sternberg Astronomical Institute, Moscow State University, Moscow, Russia*

ⁿ*Aalto University Metsähovi Radio Observatory, Aalto University Department of Radio Science and Engineering, Helsinki, Finland*

^o*Pushchino Radio Astronomy Observatory, Astro Space Center, Lebedev Physical Institute, Russian Academy of Sciences, Pushchino, Moscow oblast, Russia*

^p*Ural Federal University, Yekaterinburg, Russia*

^q*CSIRO Astronomy and Space Science, Epping, Australia*

**e-mail: nkardash@asc.rssi.ru*

Received June 30, 2016

Abstract—The RadioAstron ground-space interferometer provides the highest angular resolution achieved now in astronomy. The detection of interferometric fringes from quasars with this angular resolution on baselines of 100–200 thousand km suggests the brightness temperatures which exceed the Compton limit by two orders of magnitude. Polarimetric measurements on ground-space baselines have revealed fine structure testifying to recollimation shocks on scales of 100–250 μs and a helical magnetic field near the base of radio emission in BL Lacertae. Substructure within the scattering disk of pulsar emission on interferometer baselines (from 60000 to 250000 km) was discovered. This substructure is produced by action of the interstellar interferometer with an effective baseline of about 1 AU and the effective angular resolution of better than 1 μs . Diameters of scattering disks were measured for several pulsars, and distances to diffusing screens were evaluated. The ground-space observations of sources of the maser radiation in lines of water and hydroxyl have shown that the maser sources in star-forming regions remain unresolved on baselines, which considerably exceed the Earth diameter. These very compact and bright features with angular sizes of about 20–60 μs correspond to linear sizes of about 5–10 million km (several solar diameters).

Keywords: ground-space interferometer, very long baseline interferometry (VLBI), active galactic nuclei (AGN), quasars, pulsars, cosmic masers, interstellar scattering

DOI: 10.1134/S0038094617070085

INTRODUCTION

The RadioAstron mission is a ground-space very-long-baseline interferometry (VLBI) system, designed

for studying the structure of cosmic radio sources at ultrahigh resolution, ensured by large interferometer baselines reaching values on the order of 360000 km.

Table 1. Main GSI parameters (Kovalev et al., 2014)

Band, cm	Frequency range, MHz	Angular resolution, μ as	System equivalent flux density (SEFD), kJy		Sensitivity, mJy
			LCP	RCP	
92 (P)	316–332	530	13.3	13.5	14
18 (L)	1636–1692	100	2.76	2.93	3
6.2 (C)	4804–4860	35	11.6	–	5
1.2–1.6 (K)	18372–25132	7	46.7	36.8	16

The RadioAstron ground-space interferometer (GSI) consists of a 10-m space radio telescope (SRT), installed onboard the Spektr-R spacecraft, which revolves around the Earth in an elliptical orbit with an orbital period of 9 days. The space radio telescope operates in four wavelength bands: 92, 18, 6.2, and 1.2–1.6 cm. The GSI ensures the measurement of angular sizes of radio sources with a maximum angular resolution of 7 μ as at the wavelength of 1.3 cm and on the maximum ground-space baseline. RadioAstron also makes it possible to observe the brightest sources in observations near the orbit plane or close to the perigee passage, where the required combinations of projections of ground-space baselines are obtained. The GSI main parameters are listed in Table 1 (Kardashev et al., 2013; Kovalev et al., 2014).

In each frequency range, there are two polarization channels (LCP and RCP) of the receiver with the signal recording bandwidth of 2×16 MHz (upper and lower sub-bands). In the P band, the lower subband contains no useful signal due to input filter influence. In the C band, only one polarization channel with left circular polarization (LCP) proved to be workable. The GSI angular resolution is indicated for the maximum projected baseline as the beam FWHM. The sensitivity is given by the level of the standard deviation (1 sigma) for the integration time of 300 s in the single 16-MHz band with the use of 110-m radio telescope of the Green Bank observatory as the ground element of the interferometer.

The RadioAstron mission is performed under the general direction of the Astro Space Center of the Lebedev Physical Institute (ASC FIAN) (Kardashev et al., 2013; Burgin et al., 2015). The Spektr-R satellite control is performed by the Lavochkin Scientific and Production Association (Lavochkin Association) (Khartov et al., 2014). The spacecraft orbit determination based on the large volume of measurement and telemetry data, as well as the required calculations for control and data processing, are carried out by the Ballistics Group of the Keldysh Institute of Applied Mathematics (Zakhvatkin et al., 2014; Zaslavskiy et al., 2014). A high precision of orbit reconstruction is confirmed by the Galactic Nuclei Survey Group of the project and also by the independent VLBI-methods (Duev et al., 2015). The reception of scientific data is conducted by two specialized telemetry stations: at the Pushchino

radio astronomy observatory (Kanevskii et al., 2014) and at the Green Bank observatory (United States) (Ford et al., 2014).

The majority of the data correlation is performed using the correlator at the Data Processing Department of the ASC FIAN (Andrianov et al., 2014); in the primary data processing, the correlation centers at the Max Planck Institute for Radio Astronomy (Bonn, Germany) (Bruni et al., 2014) and at the Joint Institute for VLBI (JIVE ERIC, the Netherlands) also participate.

The contribution of large ground-based radio telescopes all over the world to the mission is of great importance for the mission implementation. This participation is provided based on competitive proposals. Some observatories allocate the observational block time at their radio telescopes under special agreements.

For coordination of development and implementation of the science program of the mission, the RadioAstron International Science Council (RISC) has been created, which consists of representatives of ASC FIAN, Lavochkin Association, researchers participating in observations at observatories, and other representatives of the international radio astronomy community. At the RISC annual meetings and teleconferences, the issues of organization and planning of scientific experiments, possible trends of research, observation results obtained in the process of mission operation, and other problems are discussed.

The science program of the RadioAstron project includes three main parts: early science program (ESP), key science program (KSP), and general observational time (GOT). As a result of the ESP fulfillment (which ended in June 2013), all capabilities of the GSI were investigated and different methods of research with GSI employment were tested, which opened the way to implementation of the enhanced science program from July 2013. Results of ESP fulfillment have been presented in (Kardashev et al., 2015). All experiments beginning from July 2013 are carried out based on proposals for research. Two-type proposals were taken for an open competition: “key space program” (most meaningful and large projects) and “general observational time”. The scientific expert examination of the submitted proposals is performed by the international review panel—RadioAstron Pro-

gram Evaluation Committee (RPEC)—and the results are approved by the head of RadioAstron project, academician N.S. Kardashev.

In this publication, we present the main results of implementation of the science program of RadioAstron mission by middle 2016. These achievements were included in the National Report on Fundamental Space Research for the Cospar-2016 symposium.

1. SCIENCE PROGRAM IMPLEMENTATION

In the context of the science program of the mission, three main types of celestial objects are studied: (i) quasars (distant galaxy nuclei), (ii) pulsars (neutron stars of the Galaxy), (iii) masers (regions of the star and planet creation in our Galaxy and other galaxies). The ground arm of the interferometer is ensured by more than 30 radio telescopes of Russia (Kvazar-KVO and Kalyazin), Ukraine (Evpatoriya, before the beginning of 2014), Australia, Great Britain, Germany, India, Spain, Italy, the Netherlands, Poland, Sweden, Finland, China, South Korea, Republic of South Africa, the United States, Japan, etc. Successful results in all scientific areas are achieved. The record angular resolution of about $10 \mu\text{as}$ is obtained. Publications can be found at the project website: <http://www.asc.rssi.ru/radioastron/publications/publ.html>.

2. MAIN SCIENTIFIC RESULTS OF STUDYING EXTRAGALACTIC OBJECTS

2.1. Observations of Quasar 3C 273 with RadioAstron: Challenging the Brightness Temperature Limit

The energy losses for the inverse Compton effect impose an upper limit on a brightness temperature of the emitting plasma of about $10^{11.5}$ K. The relativistic amplification or Doppler boosting of radiation can increase of the observed brightness temperature, but not much higher than a value of $10^{12.5}$ K.

Observations of the quasar 3C 273 on baseline projections that reach 171000 km were performed, which detected the presence of a structure on scales of up to $26 \mu\text{as}$ (2.7 light months) with a brightness temperature more than 10^{13} K. The results obtained are shown in Fig. 1. These measurements challenge our modern understanding of the nonthermal continuous emission in the vicinities of supermassive black holes and require much higher jet velocities than the observed ones. Other possible explanations include the continuous plasma reacceleration at a distance of a few parsecs from the central engine, radiation of relativistic protons, etc. (Kovalev et al., 2016).

Apart from 3C 273, measurements of brightness temperatures of many other sources are conducted within a survey of active galaxy nuclei. At the ground-space baselines, 160 quasars have been successfully detected to date. Values of measured brightness temperatures extend up to 10^{14} K and even higher. This

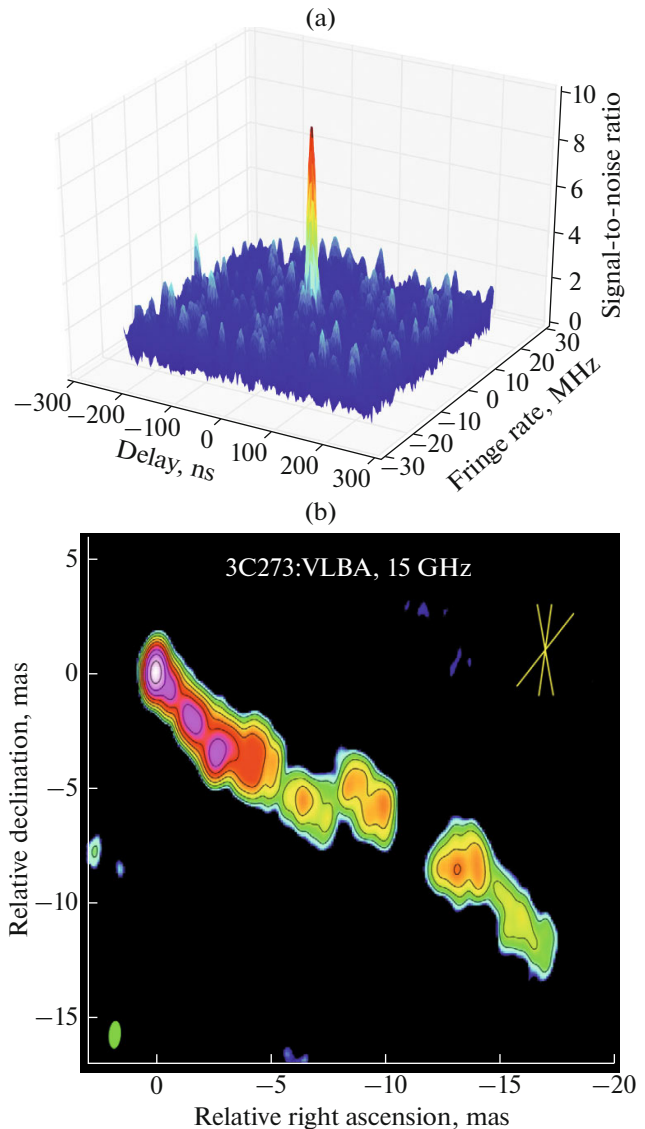


Fig. 1. (a) Response of the RadioAstron interferometer (SRT–GBT) at a frequency of 22 GHz from observations of the quasar 3C 273 on February 2, 2013 on the baseline projection length of $7.6 G\lambda$. A ratio of the interferometric response amplitude to the average noise amplitude is shown as a function of residual delays (in nanoseconds and millihertz). The probability of false detection is less than 10^{-6} . (b) A map of brightness distribution from VLBA observations of the quasar 3C 273 at 15 GHz at epoch of February 10, 2013, with the intensity peak of 3.2 Jy/beam , noise level of 1.4 mJy/beam , and beam size (green ellipse at the bottom, on the left) of $1.21 \times 0.53 \text{ mas}$. Equal intensity contours are drawn with a $\times 2$ step and a start from a level of 0.25% of the peak value. Yellow lines show a range of position angles of the ground-space baselines with the RadioAstron, implemented in the observations: 10° , -8° , and -38° .

result contradicts the possibility of equipartition between the energy density of relativistic particles and a magnetic field in nuclei of these objects. It makes us rethink our understanding of the mechanism of quasar-nuclei radiation, and significantly corrects the

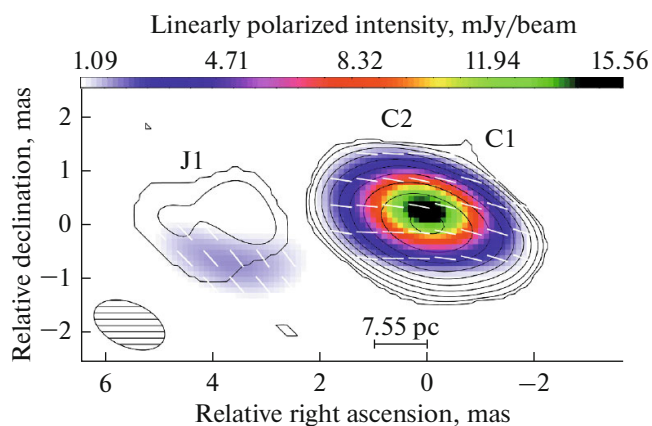


Fig. 2. Map of distribution a total (contours) and linearly polarized (colored halftones) flux of radio emission from the quasar 0642+449 at a wavelength of 18 cm. Vectors in white color indicate the orientation of the electric vector of the linearly polarized emission.

previous and current results of VLBI surveys of active galaxies, carried out at ground-based radio interferometers.

2.2. Extreme Brightness Temperatures and Refractive Scattering of the Substructure in 3C 273 with RadioAstron

Above, we discussed the detection of the quasar 3C 273 by RadioAstron on interference baselines of up to 171000 km, which suggest brightness temperatures exceeding the expected limits of the “inverse Compton catastrophe” by two orders of magnitude. We have shown that, at 18 cm, these estimates, probably, arise due to the existence of a refractive substructure caused by scattering in the interstellar medium. The scattering properties are used for estimation of the true brightness temperature amounting to 7×10^{12} K. This brightness temperature is approximately 15 times below the estimates obtained regardless of the substructure. This temperature agrees with the expected theoretical limits. With observations at a wavelength of 6 cm, the substructure considerably affects the measured values, but, in this case, provides the brightness temperature comparable with values obtained in the models which do not take the substructure into account. At a wavelength of 1.3 cm, the substructure has no influence on the extremely high brightness temperatures obtained, which are roughly 10^{13} – 10^{14} K.

Eventually, our results assume that the brightness temperature of 3C 273 grows with frequency, reaching a maximum near the 20 GHz, which coincides with the frequency of a spectral roll-off. We also detected that for the assumed Gaussian source, the estimate of the refractive substructure on the single very-large baseline determines an absolute minimum of brightness temperature, if the scattering properties along the

given line of sight are known, and that this minimum exactly approximates the apparent brightness temperature for a wide range of values of the radiant flux density. Details are given in (Johnson et al., 2016).

2.3. VLBI Mapping of Polarized Radio Emission of the Distant Quasar 0642+449 at a Frequency of 1.6 GHz

The polarization of radio emission on sub-milliarcsecond angular scales contains important data for understanding the magnetic field structure in the inner regions of jets and in closest neighborhoods of supermassive black holes at centers of active galaxies. The space VLBI observations provide the unique possibility for polarimetric mapping with the sub-milliarcsecond angular resolution and studying the magnetic-field properties in active nuclei of galaxies on scales less than 10^4 Schwarzschild radii.

The space VLBI observations of the high-redshift quasar TXS 0642+449 (OH 471), performed at a wavelength of 18 cm (frequency of 1.6 GHz) in the context of the early science program of RadioAstron mission, were used to test the operation of the orbiting space radio telescope in the polarimetric mode of observations for development of a methodology for carrying out the full Stokes polarimetry with the space VLBI at a frequency of 1.6 GHz, and for studying the polarized emission of the observed object on sub-milliarcsecond scales.

It is found that the amplitude of the SRT instrumental polarization at 18 cm is no more than 9%, showing a high reliability of the polarization mapping with the RadioAstron at this wavelength. This result (Lobanov et al., 2015) also is confirmed on the basis of statistical analysis of the data of survey of active galaxy nuclei in the RadioAstron project (Pashchenko et al., 2015).

The 0642+449 polarization image with a resolution of 0.8 mas has been obtained giving a fourfold improvement in comparison to the space VLBI observations at the same wavelength (Fig. 2). The image shows a compact structure of the core–jet type with a low ($\approx 2\%$) polarization level and a predominantly transverse magnetic field in the nuclear region. A complex structure of the nuclear region is detected with two bright features which, probably, correspond to a jet base and a strong recollimation shock. The maximum brightness temperature in the jet base was 4×10^{13} K. The results are published in (Lobanov et al., 2015).

2.4. First-ever Image of an Active Galaxy with Extreme Angular Resolution of 0.4, Obtained in Both Total Intensity and Linear Polarization at a Wavelength of 1.3 cm

The Spektr-R Russian space radio telescope together with 15 ground-based radio telescopes from

Russia (Kvazar–KVO array), Europe, and the United States, when observing the nucleus of the active galaxy BL Lacertae, yielded images with the highest-ever angular resolution in astronomy. Peculiarities of a structure of jets (giant outflows of substance with a length of up to several light years, which are ejected by the supermassive black hole at the center of this galaxy) could be recovered, and the magnetic-field structure could be reconstructed.

During the session of BL Lacertae observations, carried out at the shortest interferometer wavelength (1.3 cm), the record angular resolution— $21 \mu\text{as}$ —was achieved (Fig. 3). The object was a blazar with a supermassive black hole at the center. The black hole is surrounded by a disk of plasma heated to temperatures of a billion degrees. Powerful magnetic fields and high temperatures form the jets. Theoretic models predicted that, due to rotation of the black hole and accretion disk, magnetic field lines must form spiral structures, which, in turn, accelerate material flow in jets. We managed to see these spiral structures of the magnetic field, as well as the shock zones in the region of jet formation, which has allowed us to better understand how these radiation sources (the most powerful in the Universe) work. The galaxy core proved to have an extremely high brightness temperature. If we tried to reproduce these physical conditions on the Earth, then we would obtain a zone with a temperature of more than trillion degrees. These results are published in (Gomez et al., 2016).

2.5. Multi-frequency Mapping of a Jet in the Distant Quasar 0836+710

The radio source S5 B0836+710 is a powerful weakly polarized quasar detected at redshift 2.17, which corresponds to a photometric distance of 16.9 Gpc. In it the powerful extensive and one-sided jet on scales of parsecs and kiloparsecs is observed. The source morphology shows the presence of the plasma instability in it. The jet images, obtained using RadioAstron at 18, 6, and 1.3 cm, demonstrate a complex and twisted structure, which was unobserved in previous surveys at the ground VLBI arrays. In images, obtained at the ground-space baselines at 22 GHz (Fig. 4), the intermittent ejection can be seen with the apparent signs of effects of the transverse resolution and transverse asymmetry of the jet, which can be interpreted as proof of the important effect of limb-brightening and/or as a result of the plasma-instability propagation along the jet. Figure 4 well demonstrates advantages of the detailed ground-space VLBI image in comparison to the image obtained on ground baselines. The results will be published in the *Astronomy and Astrophysics Journal*.

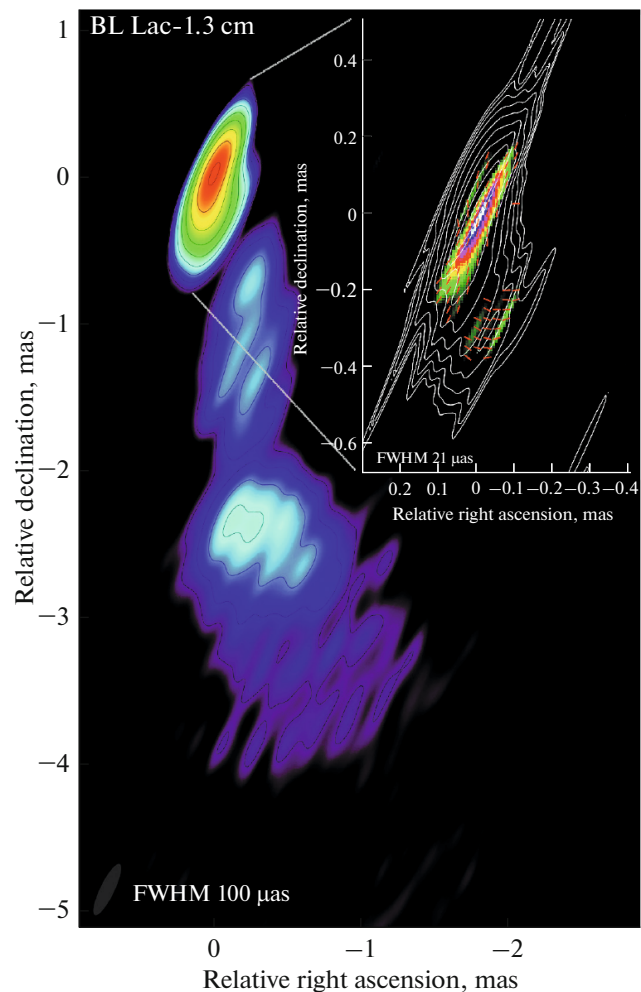


Fig. 3. Polarimetric VLBI images of the object BL Lac, obtained using the RadioAstron on November 10–11, 2013, at a wavelength of 1.3 cm, recovered with different weighting of data of the visibility function. The so-called natural weighting makes it possible to obtain the map with the lower resolution, but more sensitive to the extended regions (total intensity is shown by color and black contours, the beam has a size of $100 \mu\text{as}$). The map, obtained with the “super-uniform” weighting, is given at the inset in the right corner (total intensity is shown by white contours, linearly polarized flux is highlighted by color, position angles of the electric vector are shown by red strips, the receiving beam is $21 \mu\text{as}$).

2.6. Fine Structure of an Image of the Nearby Galaxy 3C 84, Obtained with Record Linear Resolution

In the context of fulfillment of the key science program on studying nearby galaxies, an image of the radio source 3C 84 in the giant elliptical galaxy NGC 1275 was successfully obtained with the highest angular resolution. The galaxy is located at a distance of 75 Mpc; the angular size of 1 mas corresponds to only 0.3 pc. Owing to this, the object is one of the best candidates for studying a jet near the central supermassive black hole with the highest level of spatial detail. The results

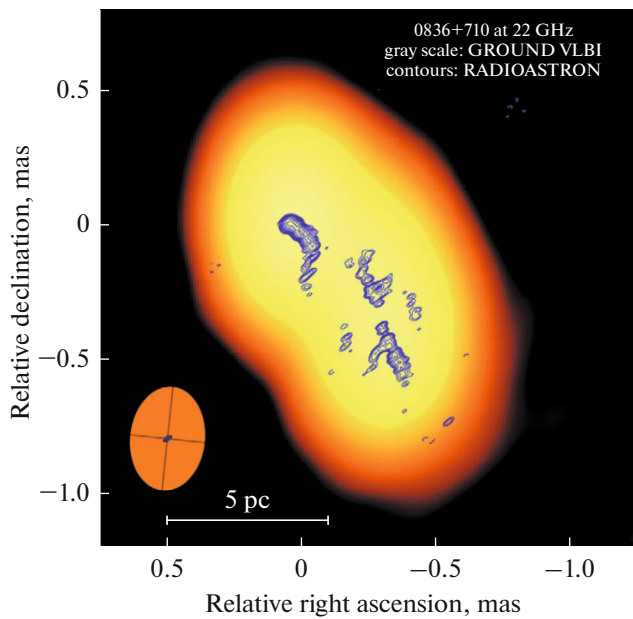


Fig. 4. Image of 0836+710, obtained using the RadioAstron at a frequency of 22 GHz (contours), imposed on the image received on the ground baselines (color).

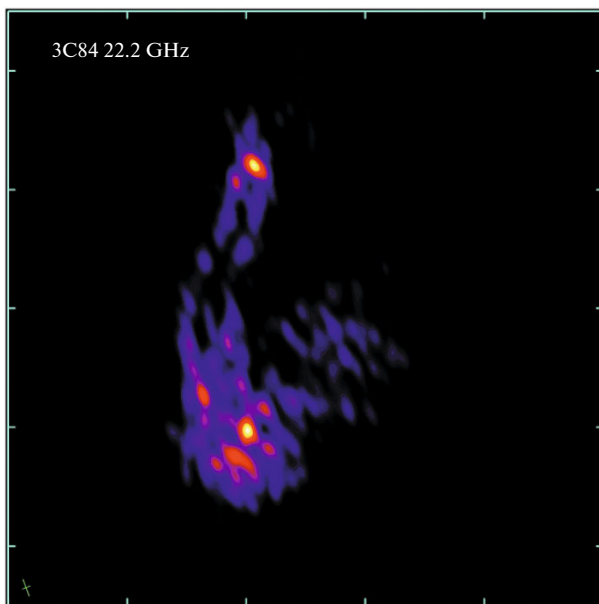


Fig. 5. A map of the nearby galaxy 3C 84, obtained in the total intensity at 22 GHz at the RadioAstron ground-space interferometer with the extreme resolution. The receiving beam of the interferometer is indicated in the left lower corner with a size of $150 \times 70 \mu\text{s}$. The visible image from north to south (from top to bottom) occupies in projection a size of 1.2 pc.

obtained will allow the better understanding of processes of formation of jet radio-emissions in galaxies.

Mapping at frequencies of 5 and 22 GHz was conducted with the ground array of 25 telescopes, including the European VLBI Network together with the Russian Kvazar–KVO, Kalyazin, the Korean VLBI

array, the American telescopes GBT, VLBA, and phased VLA. A signal of the ground-space interferometer was successfully recorded for a range of projected baselines from 0.2 to nearly 7 Earth diameters in both bands. The image obtained is presented in Fig. 5.

A central region of 3C 84 has a complex structure on sub-milliarcsecond scales. A bright spot above (north), which is the galaxy core, and a feature below (south), which moves at the sub-luminal speed along the curved trajectory, are highlighted. The image demonstrates a substructure of these regions with a unique detail. For the first time, a counter-jet (ejection in the north direction) has revealed itself clearly on the subparsec scale. The jet and counter-jet are resolved transversely, an angular resolution of the map is approximately $50 \mu\text{s}$ or 500 Schwarzschild radii.

The data on the jet structure in its base allow for studying in detail a process of jet formation in the region of the central supermassive black hole and accretion disk. The limb-brightening for the jet and counter-jet can be seen; it is an important unique result for understanding of the ejection nature. It points to the plasma-flow stratification—the effect that is extremely rarely visible in direct observations. Southward, at the jet end, a spot is highlighted, its brightness proved to be extreme for so great a distance from the central engine of the galaxy. As a result, researchers noted the effective heating of the relativistic plasma due to the interaction with the environment at the shock front. These results will be published in works by G. Giovannini et al. and Savolainen et al.

2.7. Observations of PKS 1954-388 and Detection of Its Radiation by RadioAstron at a Baseline of 80000 km

Within a survey of active galaxy nuclei with the RadioAstron, the significant signal detection was obtained on the baseline projection of 6.2 Earth diameters, which corresponds to a brightness temperature of 5.9×10^{12} K exceeding considerably the Compton catastrophe limit. This indicates that the Doppler boosting of the radiation and the significant excess of the energy density of relativistic particles over the magnetic field take place.

The observations were performed on August 23, 2012, at a frequency of 1.66 GHz with Australian radio telescopes Parkes and Mopra. Results of multiband investigation in the radio-, UV-, X-ray-, and gamma-ray-ranges were successfully interpreted in the context of the one-zone synchro-Compton model (see in more details (Edwards et al., PASA, in press)). The behavior of the correlated flux density with increasing the baseline projection is shown in Fig. 6.

3. SCIENTIFIC RESULTS
OF PULSAR STUDIES

3.1. Probing the Interstellar Plasma by Giant Pulses
of the Crab Nebula Pulsar

Giant pulses (GP) of the Crab Nebula pulsar (B0531+21) were observed in the RadioAstron project within the investigation of effects of radio-emission scattering on the interstellar medium. From 2011 to 2015 inclusive, nine observations were carried out. A list of all observations of the Crab Nebula pulsar is presented in Table 2. In this case, for the first time in the radio interferometry observations of giant pulses of the Crab Nebula pulsar, the interference responses were obtained on the ground-space baselines of up to 150000 km in observations jointly with the space radio telescope of the RadioAstron mission. An example of interference lobes is given in Fig. 7. A maximum flux density of the recorded giant pulses reached a value of 100000 Jy. For each epoch of observations, the scattering parameters (time of scattering, decorrelation bandwidth, angular size of the circle of diffusion, radius of diffraction spot, distance to the effective diffracting screen) were measured, and also phase structure functions depending on time were analyzed. Parameter measurements were conducted on assumption of the theory of a single thin effective scattering screen. All measurement results are listed in Table 3.

For each observation, our estimates of a distance to the scattering screen provide different values. During the very first session of observations (RAFS01), a distance to the screen corresponded to the case of homogeneously distributed scattering substance along the line of sight. In a different time, it was seen that the scattering dominated in regions close to the Crab nebula.

The previous studies already have shown the presence of this two-component scattering: the scattering in the region close to the Crab nebula and the extensive component caused by the interstellar plasma. For example, it was shown in (Karuppusamy et al., 2010) that for six hours of observations, for the Crab nebula pulsar, the noticeable changes were revealed in the

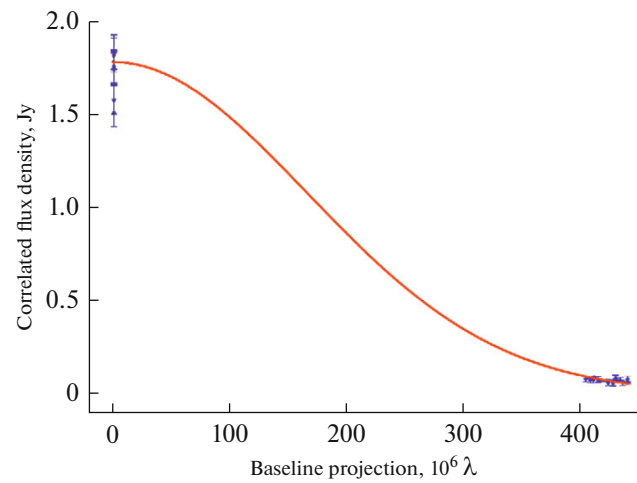


Fig. 6. Results of measurements of the correlated flux density on the ground and ground-space baselines during observations of the quasar PKS 1954–388 at the Parkes, Mopra, and RadioAstron telescopes at a wavelength of 18 cm are highlighted in blue. The red curve is a result of fitting within the assumption on the Gaussian distribution of the intensity of an emitting component.

pattern of scattering and the dominating scattering region was located in its neighborhood.

The propagation of giant pulses with the specified structure through the scattering medium with the characteristic decorrelation bandwidth was simulated. This approach made it possible to consider the influence of the GP structure on the measurement of the decorrelation bandwidth and on the structure of the visibility function. The observed quasi-regular structures in the visibility function for individual giant pulses indicate that there are strong unresolved bursts at a frequency of 1668 MHz in the structure of these pulses. Similar bursts previously were observed only at frequencies of above 5 GHz in the frequency range where they are not washed out by scattering. Thus, the VLBI observations of giant pulses from the Crab nebula pulsar allow us to conclude that in these pulses at a

Table 2. Schedule of observations of pulsar B0531+21, performed within the science program of RadioAstron mission over the period from 2011 to 2015

Session code	Date	Time	T, h	λ , cm	D, km	N_{GRT}
RAFS01	Nov. 14, 2011	23:00–00:00	1.0	18	46000	4
RAES04A	Mar. 2, 2012	13:00–17:00	4.0	18	145000	8
RAES04B	Mar. 6, 2012	13:30–17:30	4.0	18	128000	8
RAES04D	Oct. 23, 2012	07:00–09:00	2.0	18	113000	7
RAKS02AD	Oct. 27, 2013	06:00–09:00	3.0	18	150000	4
RAKS02AE	Nov. 2, 2013	19:30–08:40	12.0	92	57000	5
RAGS10A	Jan. 10, 2015	22:00–04:00	6.0	18	153000	5
RAGS10B	Jan. 28, 2015	21:00–03:00	6.0	18/92	140000	10
RAGS10C	Feb. 15, 2015	20:00–02:00	6.0	92	107000	2

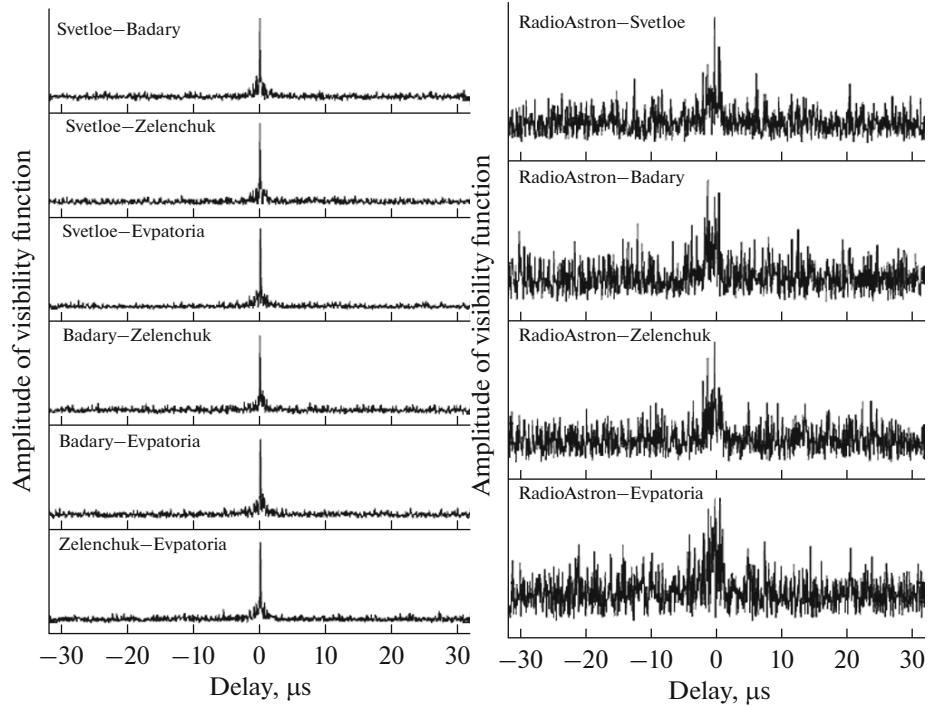


Fig. 7. Cross-correlation functions of an individual GP for different baselines, session RAFS01, the pulse of 23:21:03.74, a wavelength of 18 cm. On the left, only ground baselines are presented; on the right, only ground-space baselines are marked. On the ground-space baselines, a substructure of the circle of diffusion manifests itself.

frequency of 1668 MHz, there is a fine structure having the unresolved peaks with duration of less than 30 ns and the brightness temperature $T_b > 10^{38}$ K. On this basis, the inference can be drawn that these unresolved components with such high values of brightness temperature will propagate in the pulsar magnetosphere as strong electromagnetic waves, accelerating plasma particles, as a result of which new features are produced in the pulsar profile: HFIP, HFC1, and

HFC2, discovered by T.H. Hankins (Hankins et al., 2015).

Results of these studies are published in (Rudnitskii et al., 2016).

3.2. Distribution of Inhomogeneities of the Interstellar Plasma in the Direction towards Distant Pulsars

The radio emission from space sources undergoes scattering on inhomogeneities of the interstellar

Table 3. Measurements of scattering parameters for pulsar B0531+21 (table columns contain: (1) experiment code; (2) time of scattering; (3) angular diameter of the circle of diffusion; (4) decorrelation bandwidth; (5) a fraction of the distance from an observer to a diffusing screen; (6) the number of detected giant pulses)

Observation code	τ_{SC} , ms	Θ , mas	$\Delta\nu$, kHz	α	GP number
RAFS01	0.9 ± 0.1	1.3 ± 0.2	116.3 ± 24.5	0.36 ± 0.08	98
RAES04A	5.8 ± 0.3	0.6 ± 0.1	55.2 ± 5.9	0.94 ± 0.02	1202
RAES04B	5.5 ± 0.7	0.5 ± 0.1	41.2 ± 7.9	0.96 ± 0.03	1034
RAES04D	5.1 ± 0.5	1.2 ± 0.1	40.7 ± 4.6	0.79 ± 0.03	929
RAKS02AD	2.2 ± 0.3	1.2 ± 0.1	78.1 ± 7.9	0.61 ± 0.06	453
RAKS02AE	2340 ± 23	14.0 ± 1.4	—	0.92 ± 0.07	579
RAGS10A	1.4 ± 0.2	0.4 ± 0.1	161.1 ± 3.4	0.91 ± 0.05	1807
RAGS10B	1.5 ± 0.1	0.5 ± 0.1	70.2 ± 8.3	0.85 ± 0.04	627
RAGS10C	—	—	—	—	—

plasma. Scattering effects reveal themselves most vividly for compact sources, to which pulsars pertain. Precisely with the pulsar discovery, the manifestations of radio wave scattering on inhomogeneities of the interstellar plasma were studied theoretically and experimentally. Main effects of radio wave scattering are as follows: an increase in the measured angular size of the source τ_{SC} , an increase in the pulsar pulse width Θ_{SC} , the frequency and time modulation of the radio emission intensity with the characteristic scales $\Delta\nu_d$ and Δt_{sc} .

Simultaneous measurements of the listed above parameters for the chosen object during a sufficiently large time interval ($T > \Delta t_{sc}$) and in the fairly wide frequency band ($B_\nu > \Delta\nu_d$) make it possible to obtain the information on the structure of the interstellar-plasma inhomogeneities in the direction of this object. Advantages in studying scattering effects are provided by interferometric observations with very long baselines (VLBI): only in these observations, the scattering angle Θ_H can be measured directly. New capacities in this trend are ensured by the RadioAstron ground-space interferometer which makes it possible to obtain a high angular resolution of up to 1 mas at meter wavelengths (92 cm) and up to 0.2 mas at decimeter wavelengths (18 cm).

The interference response for the chosen pair of telescopes, which is also called the visibility function, is obtained from a set of complex cross-spectra using sequentially Fourier transforms, at first in frequency (inverse Fourier transform), and then in time (forward Fourier transform) on the time interval of integration ΔT . The visibility function $V_{AB}(\tau, f)$ is analyzed in the delay–fringe-rate diagram.

For a point source, such as a pulsar, subjected to scattering, a modulus of the visibility function, which is determined for a sufficiently large interferometer base, resolving a circle of diffusion, presents a spot of increased amplitude with dimensions of $\Delta f = 1/(2\pi\Delta t_{sc})$ and $\Delta\tau = 1/(2\pi\Delta\nu_d)$ on the fringe-rate–delay diagram, respectively. Precisely this form was demonstrated as a result of the analysis of observations of the pulsar B0329+54 on the space radio-interferometer baselines reaching 235000 km. On the smaller interferometer baselines, when both radio telescopes are located within the limits of a single diffraction spot, the visibility function has a peak at the origin of coordinates (with the correct compensation for the fringe rate and delay); the amplitude of this peak decreases with an increase in the baseline, which allows the dimensions of the circle of diffusion to be measured. A form of the interference response on large ground-space baselines is shown in Fig. 9, while a central section of the spot along the coordinate of time delay is given in Fig. 8 for different projections of the interferometer base; the uppermost curve in Fig. 8 is the section of Fig. 9. Details of studying the scattering from results of observations of the pulsar B0329+54 are published in (Gwinn et al., 2016).

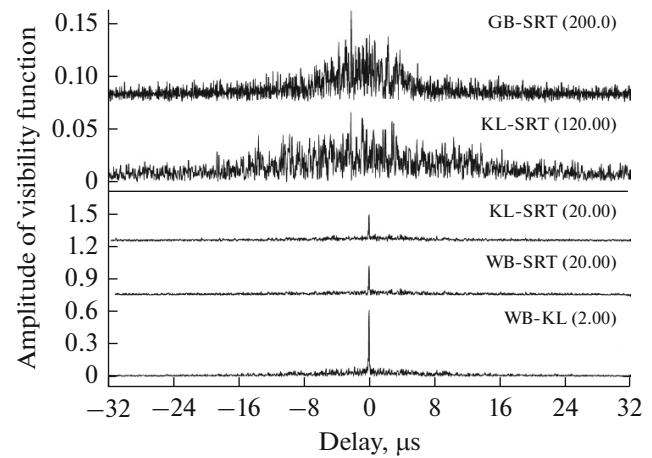


Fig. 8. Evolution of a structure of the visibility function with an increase in the interferometer base projection for the pulsar B0329+54 at a wavelength of 92 cm (324 MHz). Alongside of each curve, a combination of radio telescopes and the baseline projection value in millions of wavelengths ($M\lambda$) are depicted. For the baseline projection larger than $30 M\lambda$, a central peak of the visibility function vanishes and a structure of the circle of diffusion manifests itself. Two upper curves are shown with a tenfold increase.

The pulsar B1933+16 was observed simultaneously in two frequency bands for an hour and a half on August 1, 2013. In connection with peculiarities of SRT operation, the observations were conducted at a frequency of 316 MHz in the right circular polarization only in the upper subband, while at a frequency of 1668 MHz, in the left circular polarization in both subbands. The observations at 92 cm occurred jointly with the Westerbork Synthesis Radio Telescope (WSRT) and with the 25-m antenna of the American VLBA (Saint-Croix), while at 18 cm, the 300-m antenna in Arecibo and two 32-m telescopes in Torun and in Svetloe were used.

The diameter of the circle of diffusion at 316 MHz has been found to be $\Theta_H = 12.3 \pm 0.6$ mas, which agrees well with previous measurements by Gwinn (15.2 ± 1.3 mas), while at 1668 MHz $\Theta_H = 0.84 \pm 0.04$ mas.

Figure 10 shows the secondary spectrum at a frequency of 1668 MHz, obtained by the two-dimensional Fourier transform of the dynamic spectrum. Apart from the large central spot, individual structures can be noticed which line up with parabolic arcs with an apex at the center of the secondary spectrum. These arcs were first detected and investigated in (Stinebring et al., 2001). By the parabola shape, a position of one or several (by the number of arcs) diffusing screens can be determined independently of previous estimates, as proposed in (Hill et al., 2003).

Thus, using the RadioAstron ground-space interferometer and a number of ground interferometers, we investigated the distribution of the interstellar-plasma inhomogeneities in the direction of four distant pulsars B0329+54, B1641–45, B1749–28, and B1933+16,

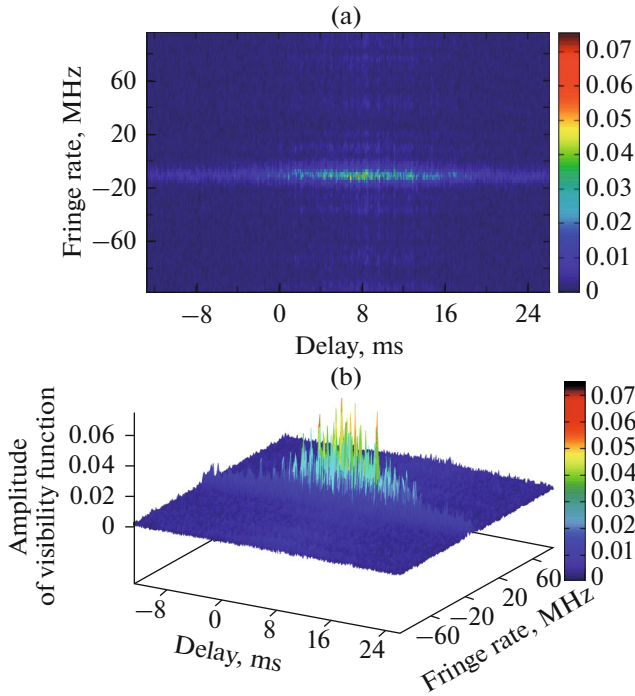


Fig. 9. Delay–fringe-rate diagram for 500-s scan of observations on November 29, 2012 (pulsar B0329+54), in the right polarization channel (the RadioAstron–Green Bank baseline): (a) two-dimensional and (b) three-dimensional presentation of the diagram.

located near the Milky Way’s plane, the radio emission of which undergoes a strong scattering. From the behavior of the normalized amplitude of the visibility function depending on a value of the baseline projection of these interferometers, the scattering angles for all pulsars were measured (Fig. 11). The time scale of broadening of the pulse scattered on the interstellar-plasma inhomogeneities was measured from the dependence of the visibility function amplitude $V(\tau)$ on the delay value or from the shape of the tail part of the mean profile of the pulse. The comparison of the scattering angle and time scale of the scattered-pulse broadening in the thin-screen model made it possible to localize a position of this screen on the line of sight from the observer to the pulsar.

It should be noted that a model of uniform distribution of the scattering plasma along the line of sight is fitted for none of pulsars. The revealed scattering screens are identified with real objects located on the line of sight towards these pulsars: G339.1-04 (PSR B1641-45) and G0.55-0.85 (PSR B174928). Additionally, from the curvature of parabolic arcs at a frequency of 1668 MHz, two screens were detected at distances of 1.3 and 3.1 kpc, the second of them can be assumed to be consistent with definitions by scattering angles. The investigations of the interstellar-plasma structure, which were performed by analysis of VLBI observations of pulsars (carried out with the RadioAs-

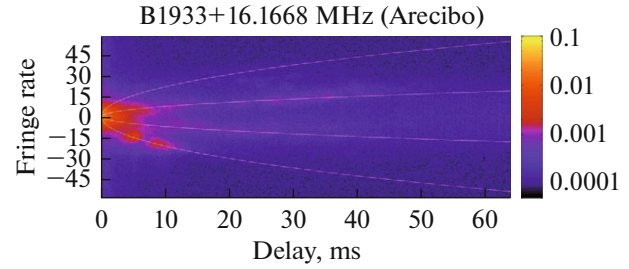


Fig. 10. Secondary spectrum for the pulsar B1933+16 at a frequency of 1668 MHz. Parabolic arcs show the presence of two effective diffusing screens at a distance of 1.3 and 3.1 kpc from the observer.

tron ground-space interferometer), have detected the particular layers responsible for the main contribution to the radio-wave scattering, and these layers are located near the Galaxy spiral arms. Results of measurements and calculations are given in Table 4. The table includes: the pulsar name, the number of correlator channels (N_{ch}), a sample rate of the correlator (δt), the time of integration (ΔT), the characteristic time of scintillations (Δt_{sc}), the decorrelation bandwidth in the spectrum ($\Delta \nu_d$), the time of scattering (τ_{sc}), an angular diameter of the circle of diffusion (Θ_H), galactic coordinates of the pulsar (l, b), a distance to the pulsar (D), and a distance to the diffusing screen (d).

3.3. Statistical Properties of a Substructure of the Scattering Disk for the pulsar B0329+54

The analysis of statistical properties of a substructure revealed in the disk of scattering of the emission from the pulsar B0329+54 at a frequency of 324 MHz at the RadioAstron ground-space interferometer is performed. The observations of this pulsar were conducted in November 2012 during four consecutive days: November 26, 27, 28, and 29; each day the session duration was 1 h. A projection of the interferometer base varied from 60 000 to 235 000 km. The 110-m radio telescope of the Green Bank observatory (United States) worked as a ground arm of the interferometer. A circle of diffusion was resolved on all baselines, i.e., the interferometric response (the visibility function) does not contain a compact feature (see Figs. 8 and 9).

A section of the interference response along the “time delay” coordinate was carried out. A structure of this section is the random variations in amplitude and phase. As a statistical characteristic of the visibility function, we used the cross-correlation function (CCF) between the visibility-function moduli, obtained in the receiver channels with different polarizations (LCP and RCP). This function $K_{\text{RL}}(\Delta T)$ smooths the deep amplitude modulation of the visibility function itself. An example of the average CCF is given in Fig. 12. It can be seen from the figure that

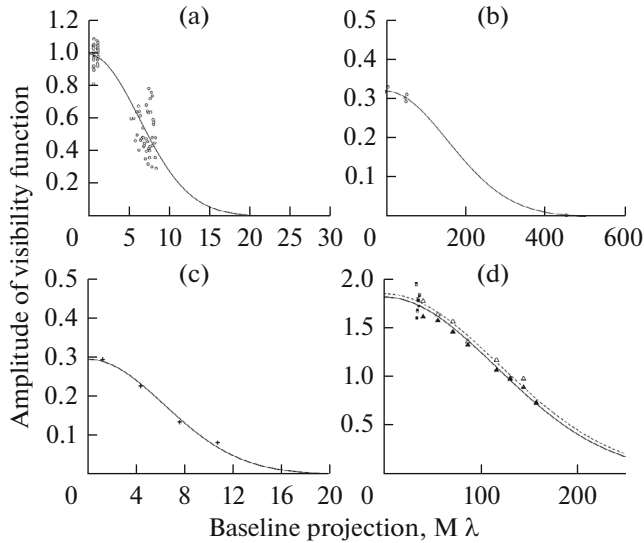


Fig. 11. (a, b) Amplitude of the visibility function vs. the baseline projection (X-axis is graduated in million wavelengths) for pulsars (a) B1641-45 (solid line corresponds to a diameter of the circle of diffusion of 27 mas, only ground baseline projections are used) and (b) B1749-28. (c, d) Amplitude of the visibility function vs. the baseline projection for the pulsar B1933+16 at frequencies of (c) 316 MHz (on the Westerbork–RadioAstron baseline) and (d) 1668 MHz (on the Arecibo–RadioAstron (triangles) and the Arecibo–Svetloe (circles) baselines; solid geometric shapes and the solid line correspond to the upper sub-band, the lower sub-band is matched by open geometric shapes and the dashed line).

there are two time scales in the CCF shape. To explain this structure, a theoretical formula was derived which was based on assumption that a transfer function of the medium comprises two exponential components

$$G(\tau) = A_1 k_1 \exp(-k_1 \tau) + A_2 k_2 \exp(-k_2 \tau).$$

The solid grey line in Fig. 12 shows the curve for out theoretical formula applied to approximation of the real CCF. This approximation was performed for all observational 10-min scans. Figure 13 shows the distribution of the measured parameters: amplitude A

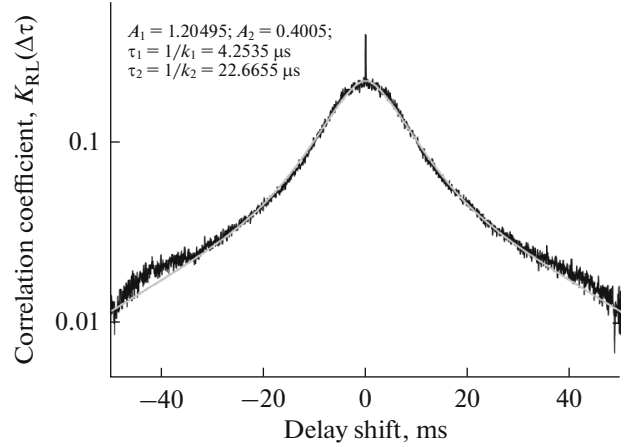


Fig. 12. Approximation of the average CCF of the visibility function by two exponential functions.

and the time constant $\tau = 1/k$. It was found that the medium transfer function has two time scales (4.1 and 23 μs) with the amplitude ratio $A_1/A_2 = 0.38$. These values do not depend noticeably on the value of the baseline projection with almost fourfold change.

A model of anisotropic scattering can serve a possible explanation of the presence of two time scales in the autocorrelation function (ACF). For this model, the ratio of time constants that we derived $k_2/k_1 = 5.5$ gives for a ratio of the scattering angles: $\theta_2/\theta_1 = 7.4$, while the ratio of amplitudes should be $A_1/A_2 = 0.40$, which is very close to the experimental value obtained. However, for four days, the baseline-projection vector changed in space by a significant angle (about 60°), and this should influence the relations of amplitudes and time constants, which was unobserved.

Another possible explanation is ordered structures, which were observed in the secondary dynamic spectra of pulsars (see Fig. 10). These structures (parabolic arcs) are assumed to arise due to the interference between substructures of the scattering disk, which were created by refraction on thin layers of the inter-

Table 4. Calculated parameters of scattering

Pulsar	N_{ch}	δt , s	ΔT , s	Δt_{sc} , s	$\Delta \nu_d$, kHz	τ_{SC} , μs	Θ_{H} , mas	l, b , $^\circ$	D , kpc	d , kpc
B1641-45	16384	0.45	115	0.20 (0.05)	0.062 (0.002)	2600 (100)	27 (5)	339.2, -0.2	4.9	3.0
B1749-28	256	5.62	225	220 (20)	410 (100)	310 (0.040)	0.5 (0.2)	1.54, -0.96	1.3	0.95
B1933+16	8192	0.35	250	—	0.25 (0.15)	600 (400)	12.3 (0.6)	52.4, -2.1	3.7	2.6
B1933+16	2048	0.35	250	41.6 (0.5)	50.4 (1.1)	3.2 (0.1)	0.84 (0.04)	52.4, -2.1	3.7	2.7 [1.3; 3.1]
B0329+54	2048	0.71	70	102 (8)	7.0 (0.8)	12 (2)	4.8 (0.8)	145, -1.2	1.0	0.5

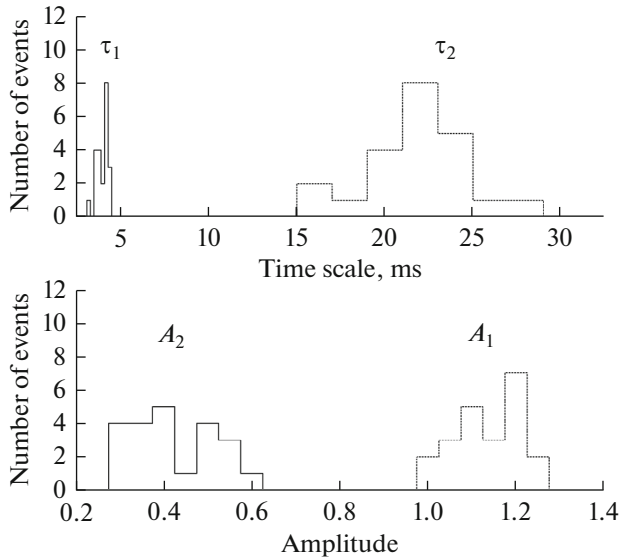


Fig. 13. Distribution of the measured parameters (time of scattering and relative contribution) for the two-component model of scattering of the radio emission of the pulsar B0329+54 at a wavelength of 92 cm.

stellar plasma. These complex structures exist in a wide range of spatial scales, which may yield two scales in ACF. However, in the secondary spectrum for the investigated pulsar B0329+54, we noticed no signs of parabolic arcs. The additional observations of this pulsar and other bright pulsars are required for this, in order to solve the puzzle of the ACF double structure. These observations are planned in the additional research program of the RadioAstron project for 2016–2018.

3.4. Studies of the Nearby Turbulent Interstellar Plasma

To separate the effects of the nearby and distant media on the radio-emission scattering of pulsars, the high spatial resolution must be available, which is ensured in our observations by the RadioAstron ground-space interferometer. The results given in this section are based on observations of scintillations of the pulsar PSR B1919+21 at a frequency of 324 MHz. PSR B1919+21 is a strong pulsar with the following galactic coordinates: a latitude of 55° , a longitude of 3.5° , and the dispersion measure $DM = 12.43 \text{ pc/cm}^3$. A distance to the pulsar was evaluated as 1 kpc based on the model by Cordes and Lazio (Cordes and Lazio, 2003). From observations of the intrinsic motion of the pulsar, its velocities in two coordinates were obtained in (Zou et al., 2005): $\mu_\alpha = 17 \pm 4 \text{ mas/yr}$ and $\mu_\beta = 32 \pm 6 \text{ mas/yr}$.

The RadioAstron 10-m space radio telescope, the 110-m telescope in Green Bank (GBT), and Westerbork (WSRT) participated in the observations. The

frequency band of 316–332 MHz was recorded with the single-bit digitization for data from the spacecraft and the two-bit digitization for ground telescopes. The primary processing was performed at the ASC FIAN correlator (Andrianov et al., 2014) with the use of the incoherent compensation for signal dispersion in the receiver band. The data were correlated with the utilization of 512 frequency channels in two selected (on-pulse and off-pulse) windows of the pulsar each with a width of 40 ms (3% of pulsar period, $P = 1.337 \text{ s}$). The on-pulse window was aligned with the maximum of the mean profile, while the off-pulse window was chosen at a separation of $0.5P$ from the previous window. The space interferometer baseline was 60000 km.

Figure 14 shows the radio spectra of individual strong pulses with a time separation (time increases from bottom to top) in seconds. The diffraction distortions caused by radio-wave scattering are clearly seen in these spectra. These distortions have two frequency scales: a fine structure with a scale on the order of 400 kHz and the large-scale structure with a scale on the order of 1500 kHz. With a small separation in time of 11 s (Figs. 14a and 14b), the fine structure remains unchanged, while on the interval of 200 s (Figs. 14b and 14d), changes. The large structure retains its shape.

The correlation analysis of dynamic spectra yields the characteristic time (t_{dif}) and frequency (f_{dif}) scales of scintillations. We have obtained the scales $f_{1,\text{dif}} = 330 \text{ kHz}$ and $f_{1,\text{dif}} = 700 \text{ kHz}$ (half-width at a level of 1/2 of the corresponding function) and amplitudes of 0.84 and 0.15 for the fine and large structures, respectively. These structures are caused by the emission scattering on the distant and nearby layers of the interstellar plasma.

The analysis of the spatial coherence function for the space baseline (RA-GB) allowed the scattering angle in the plane of the observer to be estimated: $\Theta_{\text{scat}} = 0.7 \text{ mas}$. The analysis of the frequency-time correlation function for weak scintillations provided the estimates of the angle of refraction in the direction of the pulsar: $\Theta_{\text{ref}} = 120 \text{ mas}$ and the distance to the prism $Z_{\text{prism}} < 1.3 \text{ pc}$.

Useful results were obtained by the analysis of structure functions $SF(b, \Delta f, \Delta t)$. Figure 15 shows the average time (at the top) and frequency (at the bottom) structure functions (SFs) for a ground baseline, given on the log-log scale. An arrow marks a break in the frequency structure function. Slopes of the time and frequency SFs approximately differ twofold (for scales up to 250 kHz): $\beta_1 = 0.9 \pm 0.03$ for the frequency function and $\beta_2 = 1.73 \pm 0.02$ for the time function. This relation between the frequency and time structure functions corresponds to the diffractive model of the fre-

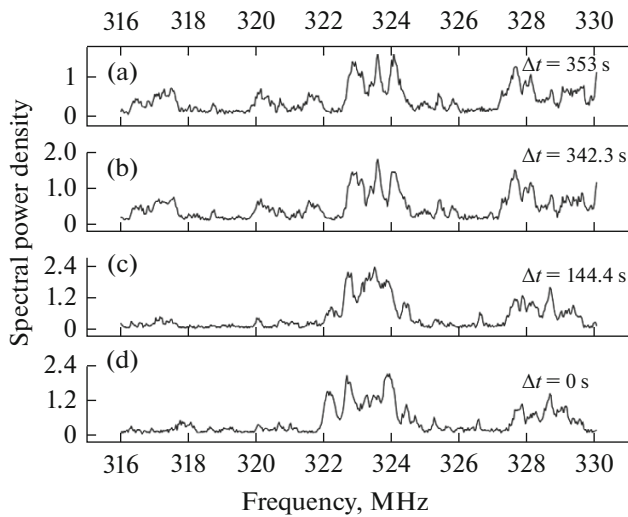


Fig. 14. Spectra of individual pulsar pulses separated in time by the depicted number of seconds from the bottom spectrum.

quency-structure formation. The index of power for the spectrum of density fluctuations of inhomogeneities is linked with the index of $SF(t)$ by the relation $n = \beta_2 + 2 = 3.73$.

Figure 16 displays average frequency structure functions for the ground (squares) and space (circles) baselines with the zero time shift. It can be seen that the levels, which the SFs reach, differ roughly by 0.2, which corresponds to the relative contribution from two frequency scales in the structure of scintillation spectra. A relation of their amplitudes agrees with the fitting of a sum of two components to the average frequency correlation function for the ground baseline. For the space baseline, there is no break in the structure function; it describes the small-scale part of spectra with the relative amplitude 0.8.

Thus, the analysis of the frequency-time and structure functions allowed us to estimate the spatial distribution of the interstellar plasma along the line of sight. The observations were shown to agree well with the presence of two screens in this direction: one of them is located at a distance of the order of 440 pc from the observer, it makes a main contribution to the pulsar (diffractive) scintillations and also determines a small-scale structure in the pulse spectra; the second one is the nearby screen at a distance of only 0.13 pc, associated with weak scintillations (large-scale structure). The Fresnel scale is equal to 2.5×10^9 cm. In addition, there is a prism behind the nearby screen, which leads to a drift of the diffraction pattern at a rate of 1.5 MHz/1000 s. We estimated a refraction angle as $\Theta_{\text{ref}} = 120$ mas and obtained an upper estimate for a distance to the prism: $Z_{\text{prism}} < 1.3$ pc. The analysis of

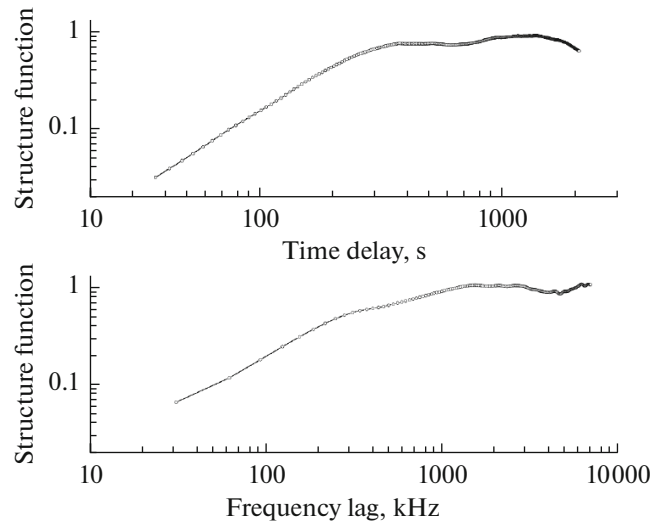


Fig. 15. Averaged time (at the top) and frequency (at the bottom) structure functions (SF) for the Green Bank–Westerbork (GB-WB) baseline, given in the log-log scale. An arrow marks a shift (300 kHz), with which a break in the frequency structure function occurs.

the spatial coherence function for the space baseline (RA-GB) made it possible to estimate a scattering angle in a plane of the observer: $\Theta_{\text{scat}} = 0.7$ mas. The analysis of the time and frequency structure functions provided a value of the index of power of the electron density fluctuations of the interstellar plasma, $n = 3.73$.

As a whole, the model of medium qualitatively repeats the medium model, which we previously used to interpret the data of observations of scintillations of the pulsar B0950+08 (Smirnova et al., 2014). However, in our case, a distance to phase screen 1 is significantly larger, the characteristic angle of scattering Θ_{scat} also is considerably greater, therefore scintillations of the pulsar 1919+21 are strong (saturated).

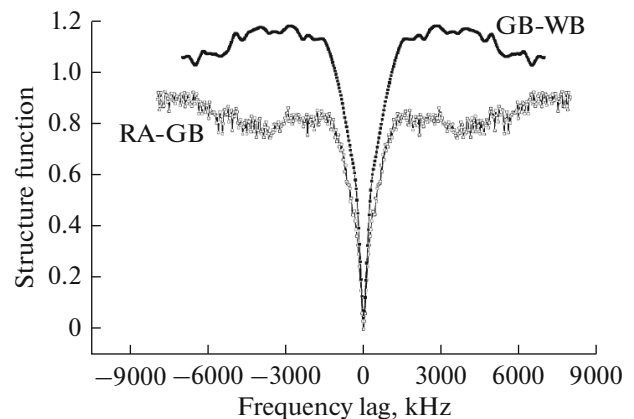


Fig. 16. Normalized frequency structure functions for the ground (GB-WB) and space (RA-GB) baselines.

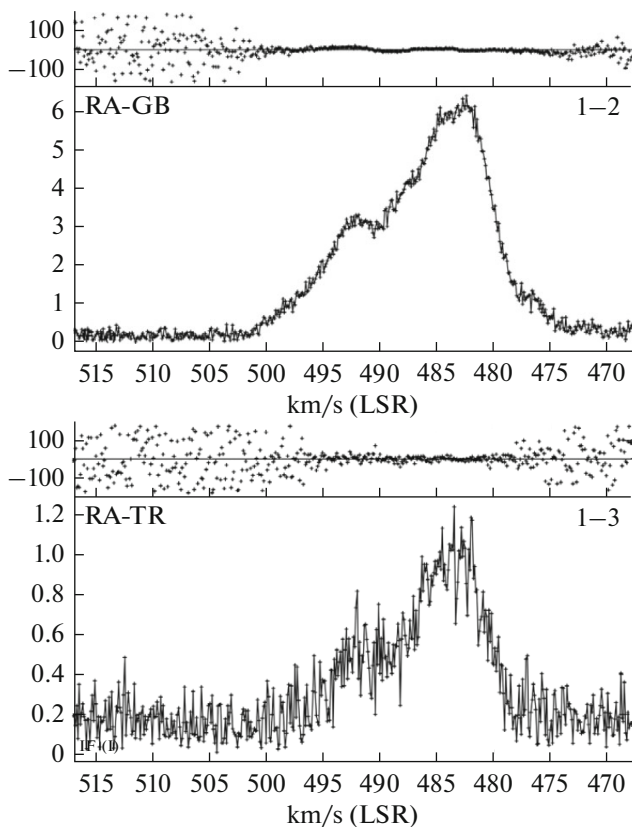


Fig. 17. Cross-correlation emission spectrum of the megamaser NGC 4258, obtained between the 10-m SRT and the ground-based telescopes: 110-m radio telescope in Green Bank (at the top) and 32-m radio telescope in Torun (at the bottom). The ordered behavior of the phase (upper part of the figure) points at a range of velocities, in which the interferometer response is recorded. In the region, where the interferometric signal from maser components is absent or lost in noises, a phase varies chaotically between the neighboring channels. The amplitude of the correlated signal in relative units and the phase in degrees are plotted along the axes depending on the spectral feature velocity in km/s with respect to the local standard of rest.

4. INVESTIGATION OF SPACE WATER MASERS AT A FREQUENCY OF 22 GHz IN THE RADIOASTRON PROJECT

4.1. First Extragalactic Masers NGC 4258 and NGC 3079, Recorded on Baselines Larger than the Earth Diameter

The galaxy NGC 4258 (Messier 106), located at a distance of roughly 24 million light years in the direction of the constellation Canes Venatici, is a prototypical galaxy in which water maser emission is observed from the gaseous accretion disk around the supermassive black hole at the center. This emission is observed in the form of numerous compact features of great luminosity, by disposition and motion of which the disk structure can be studied and a distance to the galaxy can be found.

The pumping of these masers can be fueled by the X-ray source of the central part of the galaxy. The presence of the great number of observed components is explained by instabilities and turbulence in the disk. The interferometric response from compact maser features was recorded in 2014 on the ground-space baselines between the SRT of the RadioAstron project and two ground stations: the 110-m radio telescope in Green Bank (the United States) and the 32-m telescope in Torun (Poland). A projection of the interferometer base in these observations reached nearly two Earth diameters, which corresponds to the angular resolution of about $110 \mu\text{s}$ (Fig. 17).

The second megamaser, detected by the RadioAstron ground-space interferometer, is located in the galaxy NGC 3079 (nearly 52–65 million light years in the direction of the constellation Ursa Major). Observations of NGC 3079 in November 2014 with the baseline projection of about 2.3 Earth diameters (which corresponds to the angular resolution of about $95 \mu\text{s}$) resulted in the detection of the emission of compact maser features (Fig. 18).

The successful detection of extragalactic masers has opened the door for carrying out the exploration of objects beyond the limits of the Galaxy using space interferometry. This method makes it possible to increase the angular resolution many times required for determining exact positions of masers and for studying gas movements in the near-nuclear disks of other galaxies, which is extremely important for measuring distances and studying the structure of the Universe.

4.2. Masers in Star-Forming Regions: Orion KL, W49 N, W3 (OH)

In the context of the RadioAstron key science program, the emission was detected from a very compact feature of the water maser connected with our nearest region of supermassive star formation Orion KL. The region is located at a distance of about 1370 ly from the Sun and presents a part of the molecular cloud complex in the constellation Orion. In this source, active star-forming processes occur, which are accompanied by the high-power maser emission. The compact maser feature is associated with the jet outflow from the accreting young stellar object. Estimates show that a brightness temperature of the maser emission in this object can exceed 10^{15} K.

The correlated signal was received in two experiments in November–December 2013 on the baseline between the Spektr-R space radio telescope and the ground telescopes: 40-m radio telescope in Yebes (Spain), 32-m radio telescope in Torun (Poland), and 26-m telescope near Johannesburg (Republic of South Africa). A projection of the interferometer base during the observations reached ~ 3.5 Earth diameters, sizes of radio-interferometry lobes were $\sim 63 \mu\text{s}$. At the dis-

tance of Orion KL this corresponds to a linear size of nearly 0.03 AU (about three solar diameters).

On April 27, 2015, new observations of the most distant sources of maser emission in the line of water vapor in the Galaxy (the star-forming region W49 N, located at a distance of about 36 thousand light years in the Perseus spiral arm). Several ground telescopes participated in the experiment jointly with the space telescope; a signal on the ground-space baseline was detected by two most sensitive ground antennae of the 100-m telescope in Effelsberg (Germany) and the 43-m telescope in Yebes (Spain). A projection of the interferometer base during the observations reached ~ 9.7 Earth diameters, an angular resolution amounted to the record value for observations of the water-vapor masers: $\sim 23 \mu\text{as}$.

As a result of the re-reduction of data of the early science program using the improved algorithms, the interferometric response was discovered in the session of 2012 in the direction toward the complex of bright water masers, in a direction of W3 (OH).

The correlated signal was recorded on baseline projections of up to 3.8 Earth diameters between the SRT and ground antennae in Effelsberg and Yebes; sizes of the radio-interferometry lobes were $\sim 58 \mu\text{as}$.

These observations will allow the estimation of brightness temperatures and sizes of maser sources.

4.3. Mapping of Water Masers

We present results of mapping the water masers in the star-forming region W3 IRS5 at the RadioAstron ground-space interferometer in the context of one of the key science programs of the project. Observations occurred on October 17, 2013. The European VLBI network (EVN), including the Russian telescopes of the Kvazar–KVO system, participated in the experiment jointly with the RadioAstron. A significant interference signal was received with a baseline projection of up to ~ 6 Earth diameters. This allowed an angular resolution of $36 \mu\text{as}$ to be achieved. An image of the brightest component of the maser in W3 IRS5 is presented in Fig. 19, on the left. An image of the maser spot, constructed using the data of the ground telescopes (gray contours), has an extended structure, except for a very compact feature (black contours) which is visible up to 6 Earth diameters. The analysis of data from the RadioAstron and the VERA Japanese interferometer (private communication by H. Imai) allowed the identification of a position of the compact maser features which were observed on the ground-space baselines (Fig. 19, on the right). This provides an opportunity to study a structure and physical characteristics of this star-forming region and define more exactly the mechanism of pumping. In 2015 within the RadioAstron project, the repeated mapping of H_2O masers in this star-forming region during the joint session with participation of the space radio telescope

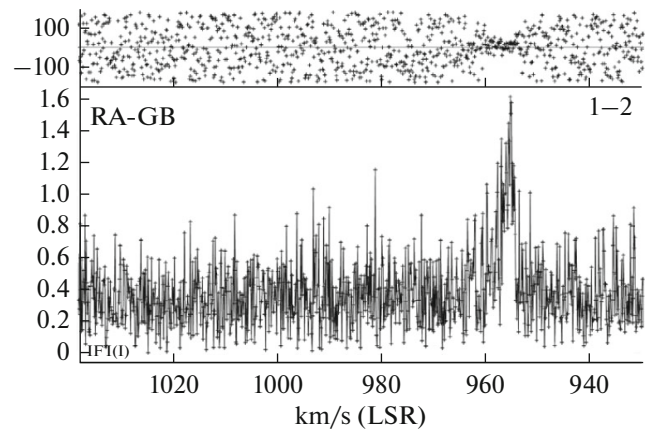


Fig. 18. Cross-correlation emission spectrum of the megamaser NGC 3079, obtained between the 10-m SRT and 110-m radio telescope in Green Bank on November 14, 2014, a maximum baseline projection was 2.3 Earth diameters (designations of axes are the same as in Fig. 17).

and the ground array of EVN telescopes was performed to obtain a position of compact features, their sizes, shapes and to compare the data with the mapping data of 2013.

For the time of the interferometer operation, more than 135 observational sessions were carried out, during which 19 (7 with success) masers in star-forming regions of the Galaxy, 8 masers (0 with success) in envelopes of stars of late types and 4 (2 with success) extragalactic sources of maser emission were observed (in all: 31 objects, 10 with success). In 24 sessions, the maser emission was recorded on the baseline projections appreciably exceeding the Earth diameter.

4.4. Thin Spatial Structure of the H_2O maser in the Globule IC 1396 N: Disk or Jets?

The globule IC 1396 N, located at a distance of 750 pc, was chosen for investigation at the ultrahigh resolution. In this region, the active formation of intermediate-mass stars is observed, and several young stellar objects and molecular outflows are detected. In the direction of the brightest young stellar object IRAS 21391+5802 ($460L_{\odot}$), the strong H_2O maser is observed, the monitoring of which has been carried out for more than 20 years. Previously, several interferometric studies of the H_2O maser were performed, and its images were obtained at resolutions of 0.5–100 mas. Based on the analysis of maser maps, a model of the precessing disk is proposed; nevertheless, the interpretation of the main data remains ambiguous (Slysh et al., 1999). It was expected that observations with (3–30 times) higher resolutions than in previous investigations will allow the source kinematics and dynamics to be clarified.

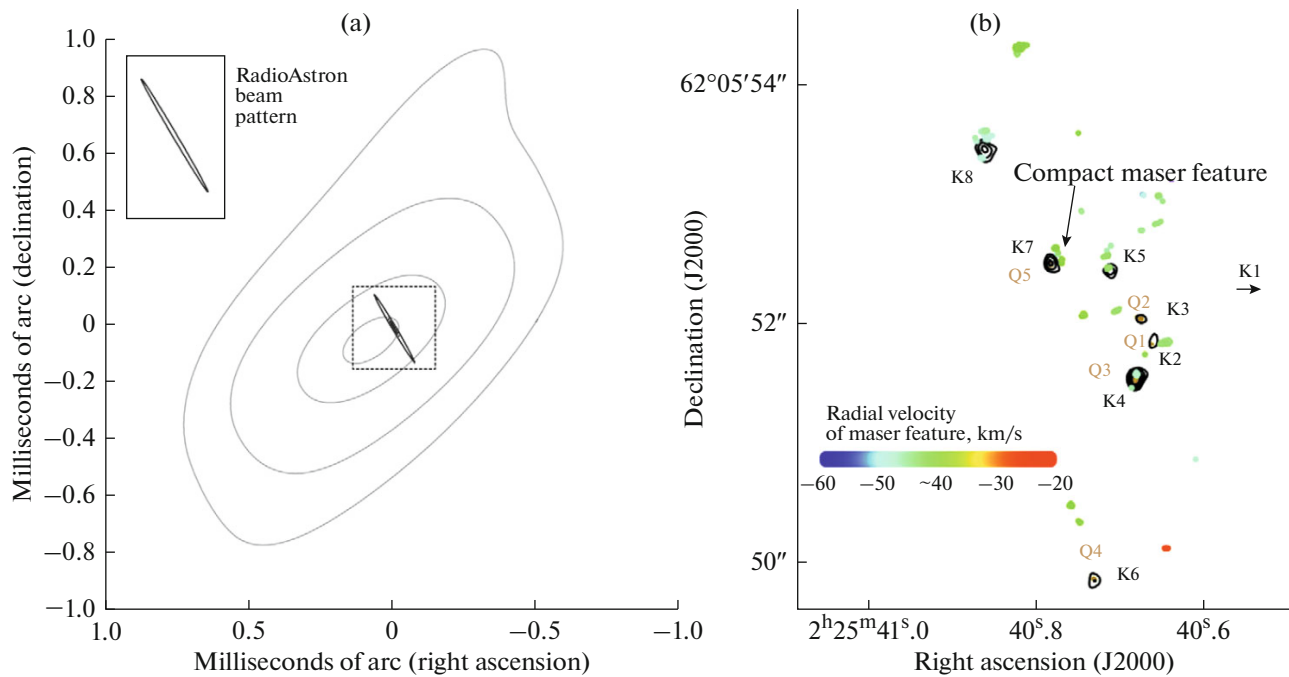


Fig. 19. Star-forming region W3 IRS5. (*On the left*) Contour plot of the brightest maser spot in the line of H_2O , recorded on the ground-space baselines (the data are received during the joint session on October 17, 2013, with the European VLBI network including the Kvazar–KVO stations). The synthesized beam pattern of the ground-space interferometer is shown in the upper left corner of the image. (*On the right*) Map of distribution of maser features in W3 IRS5, obtained in observations of the VERA Japanese interferometer (data from H. Imai). The brown and black contours show the distribution of brightness of the 7-mm and 13-mm continuous radiation. A position of the brightest compact feature, detected at the RadioAstron, is shown with the arrow.

In 2014, five sessions of observations of IC 1396 N were performed with the RadioAstron space telescope and a network of ground telescopes (Table 5).

In these observations, the source showed a strong variability: in July (during the session with the shortest ground-space baseline of ~ 2.3 Earth diameters and an angular resolution of 0.1 mas), the maximum density of a flux from the source, measured at a single telescope, was 5 Jy, while in December (during the session with a ground-space baseline projection of about 5.1 Earth diameters and an angular resolution of 0.03 mas), it was 51 Jy. The spectrum obtained in the second session (b) of observations with the best coverage of the uv-plane is given in Fig. 20a.

The source was not detected on the ground-space baselines. A lack of the signal detection on baseline

projections of more than 2.5 Earth diameters points at the lower limit (the maser size $L > 0.3$ AU) and the upper limit (brightness temperature of 6.25×10^{12} K).

Positions and fluxes of maser features were obtained from the maps constructed by the fringe-rate method from data of observations on ground baselines. The H_2O maser map is obtained, which indicates that there is a powerful material ejection from a protostellar object. Four new streamlined groups of spots (2–5, central part of the spectrum) are detected. In this case, groups 2 and 5 coincide spatially, while groups 3 and 4 were unobserved in 1996 and, probably, were the jets which formed over a period of 18 years between the observations in 1996 and in 2014 (Fig. 20b). Comparison of positions of feature groups of 1, 4, and 3, 6 (2014) with features observed previously in 1996,

Table 5. Parameters of sessions of IC 1396 N observations

Observation code	Date	Session time, h	Ground-space baseline projections (Earth diameters)	Telescopes, participating in observations	Flux density measured at a single antenna, Jy
a	July 2014	3	2.5	Ys, Nt, Sr, Tr, Kl, RA	5
b	Oct. 2014	4	3.8	Ys, Kl, Ef, Tr, RA	12
c	Nov. 2014	1	5.9	Ef, Tr, Kl, Sv, RA	20
d	Dec. 2014	1	5.1	Ef, Sr, Kl, RA	51
e	Dec. 2014	1	3.8	Sr, Tr, Sv, Zc, RA	28

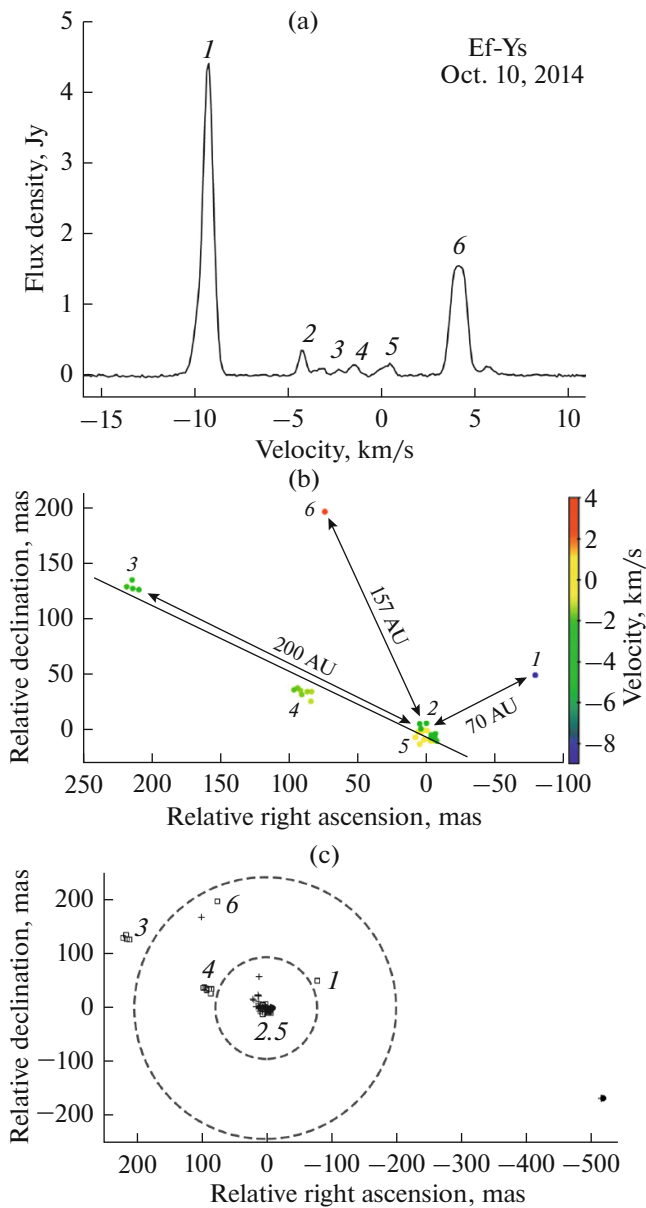


Fig. 20. (a) Cross-correlation spectrum (Stokes I), obtained in the second session of observations in 2014 (ground baseline). Numerals above the spectral features correspond to numbers of maser groups. (b) New maser spots (possible jets). A map of components of the H₂O maser in IC 1396 N, obtained in these observations (ground baseline). (c) Possible protoplanetary rings. A combined map of components of the H₂O maser in IC 1396 N, obtained in different observations and marked by: squares (these observations, ground baseline), by black circles (observations of 1996 (Slysh et al., 1999)), and by crosses (observations of 1996 (Patel et al., 2000)).

and also the available linear dependence of velocity on distances may imply that these groups are organized into two protoplanetary rings (Fig. 20c).

A regular structure (of features corresponding to the central part of the spectrum), which was observed in 1996 and previously was interpreted as a Keplerian

disk (Slysh et al., 1999), is detected also in observations of 2014, but has a smaller flux. In other words, throughout 18 years, the spatial maser structure, which is matched by the central spectrum part with the velocity spacing of nearly 1.5 km/s, is sustained on the scale of less than 20 mas, which at a distance of 750 pc, corresponds to a linear size of about 15 AU.

CONCLUSIONS

The study of objects in the Universe with a record angular resolution has allowed the research groups of the RadioAstron project to gain a number of important scientific results. We sum up briefly some of them.

(1) The analysis of results of observations of the quasar 3C 273, performed at 18, 6, and 1.3 cm on baseline projections reaching 171000 km, allowed for detection of structure in the quasar core on scales of up to 26 μ s (2.7 light months). Its brightness temperature is evaluated at a level exceeding 10^{13} K. Similar results are revealed for the large number of active galaxy nuclei. This contradicts the fact that the equality between the energy densities of relativistic particles and the magnetic field can occur in the cores of the given objects. The extreme brightness values that we have obtained make us to reinterpret the understanding of the mechanism of the nonthermal emission of quasar cores and to significantly correct the previous and modern results of the VLBI surveys of active galaxies, which are carried out at the ground radio interferometers. Additionally, we report the discovery of the effect of a substructure of refractive scattering of emission of this quasar at a wavelength of 18 cm.

(2) The space VLBI observations of the high-redshift quasar TXS 0642+449 (OH 471), performed at a wavelength of 18 cm (a frequency of 1.6 GHz) within the early science program of the RadioAstron mission, were used to test the orbital SRT operation in the polarimetric mode of observations for developing a methodology of conduction of the full Stokes polarimetry with the space VLBI at a frequency of 1.6 GHz and for studying the polarized emission of the observed object on sub-milliarcsecond scales. It is found that the amplitude of the SRT instrumental polarization at 18 cm is no more than 9%, depicting a high reliability of polarization mapping with the RadioAstron at this wavelength. A polarization image of 0642+449 at a resolution of 0.8 mas is obtained. The image shows a compact structure of the core–jet type with a low ($\approx 2\%$) polarization level and the mainly transverse magnetic field in the nuclear region. A complex structure of the nuclear region is detected which has two bright features, probably corresponding to the ejection base and the strong recollimation shock.

(3) The Spektr-R Russian SRT jointly with 15 ground radio telescopes from Russia (Kvazar–KVO array), Europe, and the United States during the observations of BL Lac produced images at a wave-

length of 1.3 cm with an angular resolution of $21 \mu\text{as}$ (the highest achieved in the history of astronomy). These measurements made it possible to discover the structural peculiarities of jets (giant outflows of matter which are ejected by a supermassive black hole at the center of this galaxy), to detect a shock in the nucleus, and to recover a spiral structure of the magnetic field.

(4) The mapping of the nearby radio galaxy 3C 84 was conducted at frequencies of 5 and 22 GHz. A signal of the ground-space interferometer was successfully recorded for a range of projections of interferometer bases from 0.2 to roughly 7 Earth diameters in both bands. For the first time, the counter-jet (outflow to the north) could be clearly seen on the subparsec scale. The jet and counter-jet are resolved transversely, the angular resolution of the map is nearly $50 \mu\text{as}$ or 500 Schwarzschild radii. Features in the jet structure near its base allow a process of the jet formation near the central supermassive black hole and accretion disk to be studied thoroughly. The limb-brightening can be seen for the jet and counter-jet; it is an important unique result for understanding a nature of the outflow. It points at the plasma-flow stratification—effect that is very rarely visible in direct observations. We note that a similar result is seen also with the RadioAstron observations of a jet in the quasar 0836+710. At a distance of more than 1 pc from the core of 3C 84, a spot is marked, its brightness proved to be extreme for this far distance from the central engine of the galaxy. Possibly, the effective heating of the relativistic plasma due to the interaction with environment at the shock front is detected.

(5) On maximum interferometer bases (50000–250000 km), a substructure of the disk of scattering of pulsar radio-emission has been detected and investigated. This substructure is due to the action of an interstellar interferometer with the effective base of about 1 AU and with the effective angular resolution better than $1 \mu\text{as}$. It was shown by the other researchers that the action of this interferometer is also applied to other radio sources (not only to pulsars) and allows the supercompact structure features to be detected in these sources. For example, a compact source was revealed at the center of the Galaxy.

(6) An angular diameter of the circle of diffusion was measured for several pulsars owing to the high-resolution capability of the RadioAstron ground-space interferometer. For these pulsars, estimates of the localization of scattering layers of the interstellar plasma are obtained; the position of these layers correlates with the Galaxy spiral structure or with particular galactic nebulae.

(7) By the method that we developed to analyze parameters of structure functions of scintillations of the pulsar radio-emission in the spectral and time domains, the plasma layers close to the Solar System were revealed on the ground and ground-space baselines, which previously were postulated for the expla-

nation of the rapid variability of compact extragalactic sources (active galactic nuclei and quasars).

(8) The measured parameters of the correlation function of the interferometric response indicate that there are two time scales in the medium-response function, which, in turn, testifies to the nonisotropic structure of interstellar-plasma inhomogeneities, apparently caused by the magnetic field influence.

(9) Observations of the water and hydroxyl masers using the RadioAstron have shown that bright features in galactic star-forming regions are resolved incompletely even on the baseline projections which significantly exceed the Earth's diameter. The record angular resolution for maser observations to date (achieved in observations of the water maser in W49N) is $23 \mu\text{as}$ (corresponds to the baseline projection of 9.7 Earth diameters).

(10) The very compact maser features with angular sizes of 20–60 μas are revealed in several star-forming regions. This corresponds to linear sizes of 5–10 million kilometers (a few solar diameters). In a number of sources, multiple components of ultra-small size are detected; this creates a foundation for studying the inner kinematics of star-forming regions.

(11) Estimates of the observed brightness temperatures lie within a range from a few $\times 10^{12}$ to 10^{16} K. In this case, a substantial loss of flux in the observed sources on space baselines is noted. This is evidence that in neighborhoods of supercompact components, the more extended regions of maser emission exist which make a significant contribution to a total flux.

ACKNOWLEDGMENTS

The RadioAstron project is implemented by the Astro Space Center of the Lebedev Physical Institute, the Russian Academy of Sciences and the Lavochkin Scientific and Production Association under a contract with the Russian Federal Space Agency in collaboration with many scientific-technical organizations in Russia and other countries. The presented results are based partially on observations performed at radio telescopes of the Institute of Applied Astronomy of the Russian Academy of Sciences. The presented investigations are partially based on the results of the Eupatoria RT-70 radio telescope (Ukraine) observations carried out by the Institute of Radio Astronomy of the National Academy of Sciences of Ukraine under a contract with the State Space Agency of Ukraine and by the National Space Facilities Control and Test Center with technical support by the Astro Space Center of the Lebedev Physical Institute, Russian Academy of Sciences. Results of optical positioning measurements of the Spektr-R spacecraft by the global MASTER Robotic Net (Lipunov et al., 2010), the ISON collaboration and the Kourvka observatory were used for the high-precision reconstruction of the spacecraft orbit in addition to the standard mission

facilities. Results are partially obtained based on observations with the 100-m telescope of the Max Planck Institute for Radio Astronomy (MPIfR) in Effelsberg and with the Medicina and Noto radio telescopes (Sardinia), operated by INAF. The European VLBI network is the joint project of the independent European, African, Asian, and North-American radio-astronomical institutes. The National Radio Astronomy Observatory of the United States is a facility of the National Science Foundation of the United States and is operated under a cooperative agreement by the Associated Universities, Inc. The Arecibo Observatory is operated by SRI International under a cooperative agreement with the National Science Foundation of the United States (AST-1100968), and in alliance with the Ana G. Mendez-Universidad Metropolitana and the Universities Space Research Association. The Australia Telescope Compact Array is a part of the Australia Telescope National Facility, which is funded by the Commonwealth of Australia and managed by CSIRO.

The presented scientific studies were partially supported by the Fundamental Research Program P-7 of the Presidium of the Russian Academy of Sciences (Subprogram “Transition and Explosion Processes in Astrophysics”) and by the Russian Foundation for Basic Research (project no. 13-02-12103).

REFERENCES

- Andrianov, A.S., Girin, I.A., Zharov, V.E., Kostenko, V.I., Likhachev, S.F., and Shatskaya, M.V., Correlator of the FIAN Astro Space Center in RadioAstron mission, *Vestn. NPO im. S.A. Lavochkina*, 2014, no. 3, pp. 55–59.
- Bruni, G., Anderson, J.M., Alef, W., Lobanov, A., et al., Space-VLBI with RadioAstron: new correlator capabilities at MPIfR, *12th European VLBI Network Symp. and Users Meeting*, Cagliari, 2014, art. ID 119.
- Burgin, M.S., Voytsik, P.A., Kutkin, A.M., Lisakov, M.M., Mironova, E.N., Sokolovsky, K.V., and Fadeev, E.N., Monitoring and control of onboard scientific equipment of the space radio telescope, *Cosm. Res.*, 2015, vol. 53, no. 3, pp. 186–192.
- Cordes, J.M. and Lazio, T.J.W., NE2001 II. Using radio propagation data to construct a model for the galactic distribution of free electrons, 2003. <http://arxiv.org/abs/astro-ph/0207156>.
- Duev, D.A., Zakhvatkin, D.A., Stepanyants, V.A., Calves, G.M., et al., RadioAstron as a target and as an instrument: enhancing the space VLBI mission’s scientific output, *Astron. Astrophys.*, 2015, vol. 573, art. ID 99.
- Ford, H.A., Anderson, R., Belousov, K., Brandt, J.J., et al., The RadioAstron Green Bank Earth Station, *Proc. SPIE*, 2014, vol. 9145, art. ID 91450B.
- Gomez, J.L., Lobanov, A.P., Bruni, G., Kovalev, Y.Y., et al., Probing the innermost regions of AGN jets and their magnetic fields with RadioAstron. I. Imaging BL Lacertae at 21 μ s resolution, *Astrophys. J.*, 2016, vol. 817, art. ID 96.
- Gwinn, C.R., Popov, M.V., Bartel, N., Andrianov, A.S., et al., PSR B0329+54: statistics of substructure discovered within the scattering disk on RadioAstron baselines of up to 235000 km, *Astrophys. J.*, 2016, vol. 822, art. ID 96.
- Hankins, T.H., Jones, G., and Eilek, J.A., The crab pulsar at centimeter wavelengths. I. Ensemble characteristics, *Astrophys. J.*, 2015, vol. 802, no. 2, art. ID 130.
- Hill, A.S., Stinebring, D.R., Barnor, H.A., Berwick, D.E., et al., Pulsar scintillation arcs. I. Frequency dependence, *Astrophys. J.*, 2003, vol. 599, pp. 457–464.
- Johnson, M.D., Kovalev, Y.Y., Gwinn, C.R., Gurvits, L.I., et al., Extreme brightness temperatures and refractive substructure in 3C273 with RadioAstron, *Astrophys. J. Lett.*, 2016, vol. 820, no. L10.
- Kanevskii, B.Z., Smirnov, A.I., Sazankov, S.V., Belousov, K.G., et al., The Earth-based tracking station. RadioAstron project, *Vestn. NPO im. S.A. Lavochkina*, 2014, no. 3, pp. 47–54.
- Kardashev, N.S., Khartov, V.V., Abramov, V.V., Avdeev, V.Yu., et al., “RadioAstron”—a telescope with a size of 300000 km: main parameters and first observational results, *Astron. Rep.*, 2013, vol. 57, no. 3, pp. 153–194.
- Kardashev, N.S., Alakoz, A.V., Kovalev, Y.Y., Popov, M.V., Sobolev, A.M., and Sokolovsky, K.V., Radioastron: main results of the implementation of the early science program in studies of astronomical objects in the universe with ultra-high angular resolution, *Sol. Syst. Res.*, 2015, vol. 49, no. 7, pp. 573–579.
- Karuppusamy, R., Stappers, B.W., and van Straten, W., Giant pulses from the crab pulsar. A wide-band study, *Astron. Astrophys.*, 2010, vol. 515, no. 36.
- Khartov, V.V., Shirshakov, A.E., Artyukhov, M.I., Kazakevich, Y.V., Vorob’ev, A.Z., Kalashnikov, A.I., Pogodin, A.V., Filippova, E.N., and Komovkin, S.V., Features of RadioAstron mission control, *Cosm. Res.*, 2014, vol. 52, no. 5, pp. 326–331.
- Kovalev, Y.A., Vasil’kov, V.I., Popov, M.V., Soglasnov, V.A., Voitsik, P.A., Lisakov, M.M., Kut’kin, A.M., Nikolaev, N.Y., Nizhel’skii, N.A., Zhekanis, G.V., and Tsybulev, P.G., The RadioAstron project: measurements and analysis of basic parameters of space telescope in flight in 2011–2013, *Cosm. Res.*, 2014, vol. 52, no. 5, pp. 393–402.
- Kovalev, Y.Y., Kardashev, N.S., Kellermann, K.I., Lobanov, A.P., et al., RadioAstron observations of the Quasar 3C273: a challenge to the brightness temperature limit, *Astrophys. J. Lett.*, 2016, vol. 820, no. L9.
- Lipunov, V., Kornilov, V., Gorbovskoy, E., et al., Master robotic net, *Adv. Astron.*, 2010, vol. 349, pp. 171–175.
- Lobanov, A.P., Gomez, J.L., Bruni, G., Kovalev, Y.Y., et al., RadioAstron space VLBI imaging of polarized radio emission in the high-redshift Quasar 0642+449 at 1.6 GHz, *Astron. Astrophys.*, 2015, vol. 583, art. ID 100.
- Pashchenko, I.N., Kovalev, Y.Y., and Voitsik, P.A., First estimate of the value of the instrumental polarization of the RadioAstron space radio telescope using the results of an early scientific program for observing active galactic nuclei, *Cosm. Res.*, 2015, vol. 53, no. 3, pp. 199–208.
- Patel, N.A., Greenhill, L.J., Herrnstein, J., Zhang, Q., et al., Proper motion of water masers associated with IRAS 21391+5802: bipolar outflow and an AU-scale

- dusty circumstellar shell, *Astrophys. J.*, 2000, vol. 538, pp. 268–274.
- Rudnitskii, A.G., Karuppusamy, R., Popov, M.V., and Soglasnov, V.A., Studies of cosmic plasma using radioastron VLBI observations of giant pulses of the pulsar B0531+21, *Astron. Rep.*, 2016, vol. 60, no. 2, pp. 211–219.
- Slysh, V.I., Val'tts, I.E., Migenes, V., Fomalont, E., et al., Protoplanetary disk and/or bipolar outflow traced by H₂O masers in IC 1396N, *Astrophys. J.*, 1999, vol. 526, pp. 236–241.
- Smirnova, T.V., Shishov, V.I., Popov, M.V., Gwinn, C.R., Anderson, J.M., et al., RadioAstron studies of the nearby, turbulent interstellar plasma with the longest space-ground interferometric baselines, *Astrophys. J.*, 2014, vol. 786, art. ID 115.
- Stinebring, D.R., McLaughlin, M.A., Becker, K.M., Espinoza Goodman, J.E., et al., Faint scattering around pulsars: probing the interstellar medium on solar system size scales, *Astrophys. J.*, 2001, vol. 549, pp. L97–L100.
- Zakhvatkin, M.V., Ponomarev, Y.N., Stepan'yants, V.A., Tuchin, A.G., and Zaslavskiy, G.S., Navigation support for the RadioAstron mission, *Cosm. Res.*, 2014, vol. 52, no. 5, pp. 342–352.
- Zaslavskiy, G.S., Stepan'yants, V.A., Tuchin, A.G., Pogodin, A.V., Filippova, E.N., and Sheikhet, A.I., Trajectory correction of the Spektr-R spacecraft motion, *Cosm. Res.*, 2014, vol. 52, no. 5, pp. 353–364.
- Zou, W.Z., Hobbs, G., Wang, N., Manchester, R.N., et al., Timing measurements and proper motions of 74 pulsars using the Nanshan radio telescope, *Mon. Not. R. Astron. Soc.*, 2005, vol. 362, pp. 1189–1198.

Translated by M. Samokhina